Low-Temperature Self-Catalytic Growth of Tin Oxide Nanocones over Large Areas

Sangmoo Jeong,[†] Matthew T. McDowell,[‡] and Yi Cui[‡,*]

[†]Department of Electrical Engineering and [‡]Department of Materials Science and Engineering, Stanford University, Stanford, California 94305, United States

ABSTRACT Nanoscale texturing has been studied for various applications, but most of the methods used to make these nanostructures are expensive and not easily scalable. Some of these methods require etching steps or high-temperature processes, which limit the processes to certain materials, such as silicon. In this study, we report a non-etching nanoscale texturing technique that allows for controlled oxidation to create tin oxide nanocones over large areas. Similar results are obtained on different substrates, such as silicon, aluminum foil, quartz, and polyimide film, and this method can be employed at temperatures as low as 220 °C in ambient pressure. This simple and scalable nanotexturing process improves the anti-reflection effect in photovoltaic devices. The light absorption of a polycrystalline silicon substrate, a widely used photovoltaic material, is increased by 30% over the wavelength range of 400−850 nm after fabricating nanocones on the surface.

KEYWORDS: nanotexturing · self-catalytic growth · nanocone · anti-reflection

Nanotextured substrates are of interest in various research areas because of their many functionalities. Recently, improved light absorption has been demonstrated for thin-film photovoltaic devices on nanotextured substrates consisting of nanowires,[1−3] nanocones,[4] and nanodomes.[5] Nanotexturing results in a graded refractive index profile of the absorber material, which causes enhanced anti-reflection properties and allows for waveguide effects in solar cells. In addition to improvements in light absorption, nanotexturing changes the wetting properties of a substrate.[6−8] As nanotexturing techniques are beginning to be used in various applications, attributes related to practical applications, such as scalability, cost, and process temperature, are becoming more critical. Thus far, the common methods used to produce nanotextured surfaces include lithography and chemical vapor deposition.[1,2,9] These methods are useful for fundamental studies but are not easily scaled to large areas: they are expensive,and the required temperatures are usually higher than 600 °C, which limits the range of compatible substrate materials. Alternatively, one scalable nanotexturing technique with silica nanoparticles was developed based on a wire-wound rod coating method.[10] It is a solution process that can be applied to a variety of substrates (including plastic), but the morphology of the nanotextured surfaces is limited to a rounded form because of the spherical nanoparticles. In order to make rough nanotextured surfaces (arrays of nanowires or nanocones), etching steps would be required. Here, we demonstrate a scalable, low-temperature technique to make nanocone structures without any etching processes: the self-catalytic VLS growth of tin oxide (SnO_x) nanocone structures by annealing a thin film of Sn at low temperatures (220−450 °C). The aspect ratio of these nanocones can be easily controlled by changing oxygen concentration and annealing temperature.

RESULTS AND DISCUSSION

When Sn is evaporated onto many rigid substrates, including silicon, quartz, and aluminum foil, the deposited Sn atoms are more strongly bound to each other than they are to the substrate,[11] and thus the thin film of Sn consists of Sn nanoislands (Figure 1a,b). The average size of these nanoislands in a 50 nm thick Sn film is approximately 200 nm × 200 nm (0.04 μm^2) (Figure 1c). If the deposited Sn film is annealed at a temperature higher than its melting point (T_m = 233 °C) in an oxygen-containing environment, Sn becomes oxidized to SnO_x. However, there are drastic differences in final morphology when annealing at different oxygen concentrations. In air, where the oxygen concentration is high (∼20%), Sn nanoislands transform into SnO_x nanoislands without any significant shape changes, as illustrated in Figure 1d. Figure 1e shows a scanning electron microscope (SEM) image of the SnO_x nanoisland film formed when a 50 nm thick Sn film was annealed at 300 °C for 3 h in air. In sharp contrast, if the Sn

* Address correspondence to yicui@stanford.edu.

Received for review April 25, 2011 and accepted June 18, 2011.

Published online June 18, 2011
10.1021/nn2015216

© 2011 American Chemical Society

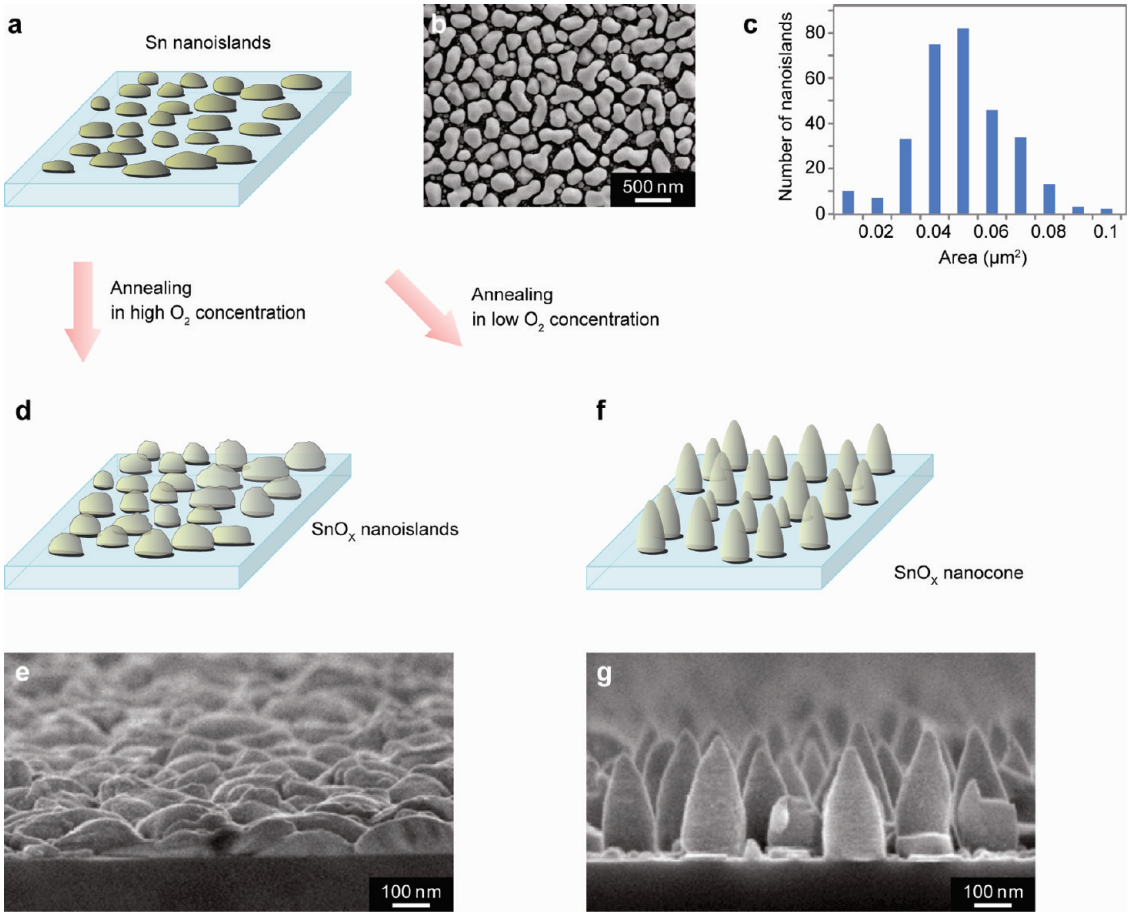

Figure 1. Design of SnO_x nanocone arrays. (a) Schematic of a Sn film that consists of disconnected Sn nanoislands. (b) SEM image of a Sn film (50 nm thick) deposited by e-beam evaporation on a silicon substrate. (c) Statistical data of the area of the Sn nanoislands in panel b. (d,e) Schematic and SEM image of the SnO_x nanoislands formed when a 50 nm thick Sn film was annealed at 300 °C for 3 h in air. (f,g) Schematic and SEM image of the SnO_x nanocones formed when a 50 nm thick Sn film was annealed at 300 °C for 3 h in a nitrogen environment with less than 100 ppm oxygen concentration.

nanoislands are annealed under the same conditions but with much lower oxygen concentration (*i.e.*, <0.1%), the resulting shape is surprisingly different: the planar Sn nanoislands are converted to SnO_x nanocones (Figure 1f). Figure 1g shows a SEM image of SnO_x nanocones formed when a Sn film with the same thickness (50 nm) was annealed for the same period (3 h) at the same temperature (300 °C) in a nitrogen gas environment with ~100 ppm oxygen concentration (hereafter called the low-oxygen environment). These SnO_x nanocones were formed over a large area (25 cm^2) of a Si substrate, as shown in Supporting Information Figure S1.

The growth mechanism of SnO_x nanocones can be explained with reference to the model shown in Figure 2a. When a Sn nanoisland is annealed above its melting point in air, the high concentration of oxygen at the Sn surface can produce a solid SnO_x layer, which fixes the shape of the nanoisland. As it is annealed for longer times, Sn atoms diffuse out to the surface to be oxidized, which results in a hollow space inside the SnO_x layer. This phenomenon is the nanoscale Kirkendall effect, which has been observed during the oxidation of various metal nanoparticles.[12−14] However, in the low-oxygen environment, each Sn nanoisland forms a liquid Sn nanodroplet when annealed above the melting point. Due to the low oxygen concentration, the solid SnO_x layer cannot be formed quickly enough to prevent the shape change of the Sn nanoisland from a flat to a spherical shape. As the liquid Sn nanodroplet is annealed for longer times, the oxygen concentration inside the nanodroplet increases and supersaturates to nucleate the solid SnO_x phase. The nucleation of solid SnO_x is favorable at the interface between the liquid Sn and solid substrate. The surface tension of the liquid Sn causes it to retain a hemispherical shape on top of the solid SnO_x, and the continuous consumption of the Sn by the formation of the SnO_x without any additional input of Sn causes the Sn droplet to shrink in size. The combined factors of high surface tension and the decreasing amount of liquid Sn as SnO_x is formed result in the formation of a tapering SnO_x nanocone structure. Since there is no introduction of a separate catalyst, this is a self-catalytic process. This process is similar to vapor−liquid−solid growth,[15−17] but in our case, the catalyst particles lose atoms during growth. Figure 2b displays SEM images of Sn films annealed for

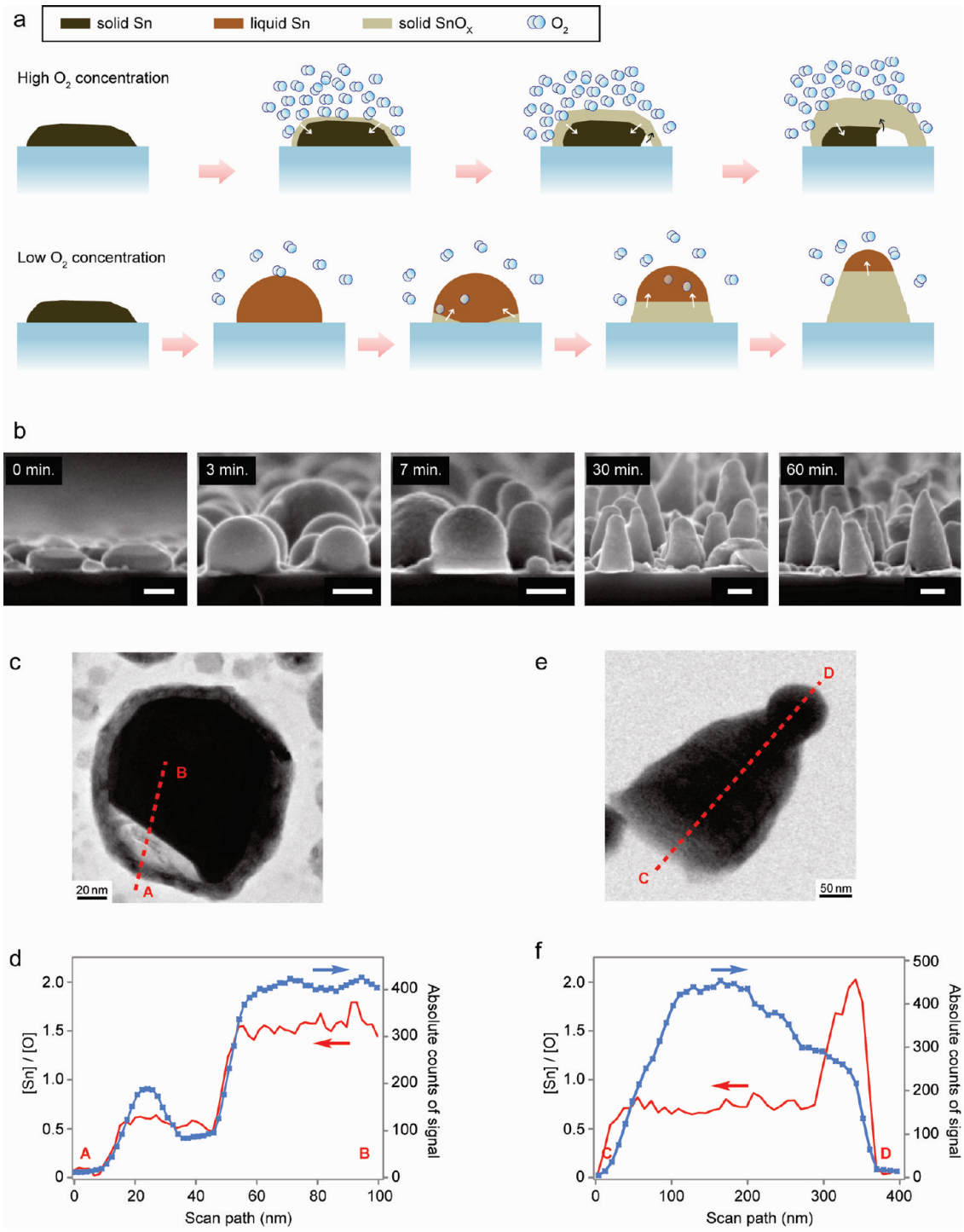

Figure 2. Proposed model of SnO_x nanocone formation and supporting data. (a) Schematics of the oxidation process of Sn nanoislands. The white arrow indicates the formation of solid SnO_x, and the black arrow shows the diffusion of Sn through the already-formed SnO_x layer. (b) SEM images of Sn films (50 nm thick) annealed at 300 °C for different time periods in the low-oxygen environment. All scale bars are 100 nm. (c) STEM image of the SnO_x nanoisland formed when a Sn nanoisland was annealed at 300 °C for 3 h in air. (d) EDS data collected along the red trace from point A to B in panel c. (e) STEM image of the SnO_x nanocone formed when a Sn nanoisland was annealed for 20 min under the same conditions as those in panel b. (f) EDS data collected along the red trace from point C to D in panel e.

different amounts of time in low-oxygen environments; these images show the process of nanocone formation. As explained above, a planar Sn nanoisland transforms into a Sn nanodroplet, and as the annealing time increases, it produces a tapered structure with a small ball on top.

To confirm the proposed mechanism, we employed scanning transmission electron microscopy (STEM). The STEM image in Figure 2c is a SnO_x nanoisland formed when a 40 nm thick Sn film was annealed at 300 °C for 3 h in air. The center of the nanoisland shows

darker contrast than the outside layer, and energy-dispersive spectroscopy (EDS) analysis confirms that the Sn to O ratio of the outside layer is ~0.5, but that of the center is much higher than 0.5. EDS data collected along the red line in Figure 2c are presented in Figure 2d. The absolute counts of the EDS data, represented by the blue trace in Figure 2d, decrease suddenly between 30 and 50 nm along the scan line, which corresponds to the bright area between the outside layer and the dark center of the nanoisland in Figure 2c. The light contrast and the sudden drop in the counts of the EDS data indicate that the bright area between points A and B in Figure 2c is a void, which can be explained by Sn diffusion during the oxidation process. In contrast, the nanocone shown in Figure 2e was formed when a Sn film with the same thickness (40 nm) was annealed at the same temperature (300 °C) for 20 min in the low-oxygen environment. EDS data were collected along the red line in Figure 2e from point C to D, and the Sn to O ratio is displayed in Figure 2f as a red trace. In the base of the nanocone, the Sn to O ratio is 0.7−0.8, which corresponds to the Sn_3O_4 phase. In the top section, the Sn signal is much stronger than the O signal. This confirms our proposed mechanism in which a solid SnO_x nanocone grows from the bottom of a liquid Sn droplet, which lifts the Sn droplet upward away from the substrate during growth of the nanocone. The gradual decrease of the absolute counts of the EDS data (the blue trace in Figure 2f) from the base (point C) to the top (point D) and the relatively constant contrast of the nanocone image indicate that there are no voids formed during growth. In addition to these data, the EDS spectra at two different spots (the top and base) of the nanocone in Figure 2e are shown in Supporting Information Figure S2. The formation of SnO_x nanocones was observed on various substrates, such as aluminum foil and quartz (Supporting Information Figure S3), and Sn films with thicknesses ranging from 20 to 200 nm form similar nanocone structures of different sizes (Supporting Information Figure S4).

The crystal structure of the nanocones was investigated with X-ray diffraction (XRD) and TEM. The XRD data shown in Figure 3a reveal that the nanocones are made up of different phases of SnO_x. As annealing time increases, the peaks that correspond to pure Sn diminish in intensity while other peaks that correspond to SnO and Sn_3O_4 increase. After 15 min of annealing, the nanocones were mostly single-crystalline, as shown by the diffraction pattern and high-resolution TEM (HRTEM) image in Figure 3b of one Sn_3O_4 nanocone. After annealing for more than 30 min, SnO_2 peaks appear in the XRD signal along with a decrease in the intensity of SnO peaks, but Sn_3O_4 peaks seem to have similar intensities. These changes of peak intensities can be explained by the TEM data presented in Figure 3c−f. The nanocones in these panels were formed after 180 min annealing, and they contain multiple phases of SnO_x. The nanocone in Figure 3c is made up of both tetragonal SnO and triclinic Sn_3O_4, as evidenced by the selected area electron diffraction pattern and HRTEM image. The nanocone in Figure 3d was found to have three stripes of Sn_3O_4 surrounded by SnO_2 structures. The EDS data collected along the nanocone in Figure 3e are presented in Figure 3f, which shows that the Sn to O ratio varies, indicating that SnO, Sn_3O_4, and SnO_2 are all present in the nanocone. It has been observed that the final oxidation state of Sn, SnO_2, can be reached through simple oxidation of SnO or through the intermediate oxidation state Sn_3O_4.[18] Therefore, as the nanocones are annealed in the low-oxygen environment for long times (*i.e.*, longer than ~1 h), phase transformations from SnO to Sn_3O_4 or SnO_2 and from Sn_3O_4 to SnO_2 occur within the nanocone body. This explains the change of peak intensities in the XRD data: the SnO peak intensity decreases, the SnO_2 peak intensity increases, and the Sn_3O_4 peak intensity remains relatively constant. This transformation seems to happen in the solid state after the nanocones are grown because the growth of nanocones is almost completed after 30 min of annealing (Figure 2b) and nanocones are generally found to be single-crystalline if observed during the initial growth process. The formation of multiple phases and phase boundaries in the same nanocone is very interesting, and there needs to be further investigation to study the phase change mechanisms involved.

On the basis of the understanding, we conducted experiments to control the shape of SnO_x nanocones by varying two parameters: oxygen concentration and annealing temperature. The nanocone formation is mainly due to the low oxygen level in the environment, which allows for the formation of liquid Sn droplets and the growth of solid SnO_x at the interface between the Sn droplets and solid substrate. The surface tension of liquid Sn, one factor that causes the tapering nanocone structure (as mentioned above), becomes greater as the annealing temperature increases[19,20] and the oxygen level in the environment decreases.[21] This could be one reason why the SnO_x nanocones formed at a lower annealing temperature are broader and shorter; similar effects are observed when the oxygen concentration increases (Figure 4a,b). In addition, the formation of nanocones is related to the interplay of the oxide growth rate and the rate of shape change upon heating as the Sn forms a liquid droplet. When a Sn film is annealed in air, a quickly formed SnO_x shell prevents the liquid Sn from changing shape. In the limiting case when there is virtually no oxygen during annealing, the Sn film balls up on the substrate before the SnO_x shell grows. If there is an intermediate amount of oxygen in the environment, the nucleation and growth of SnO_x occurs at the interface between the liquid Sn and solid substrate while a liquid ball is formed. Therefore, the change in

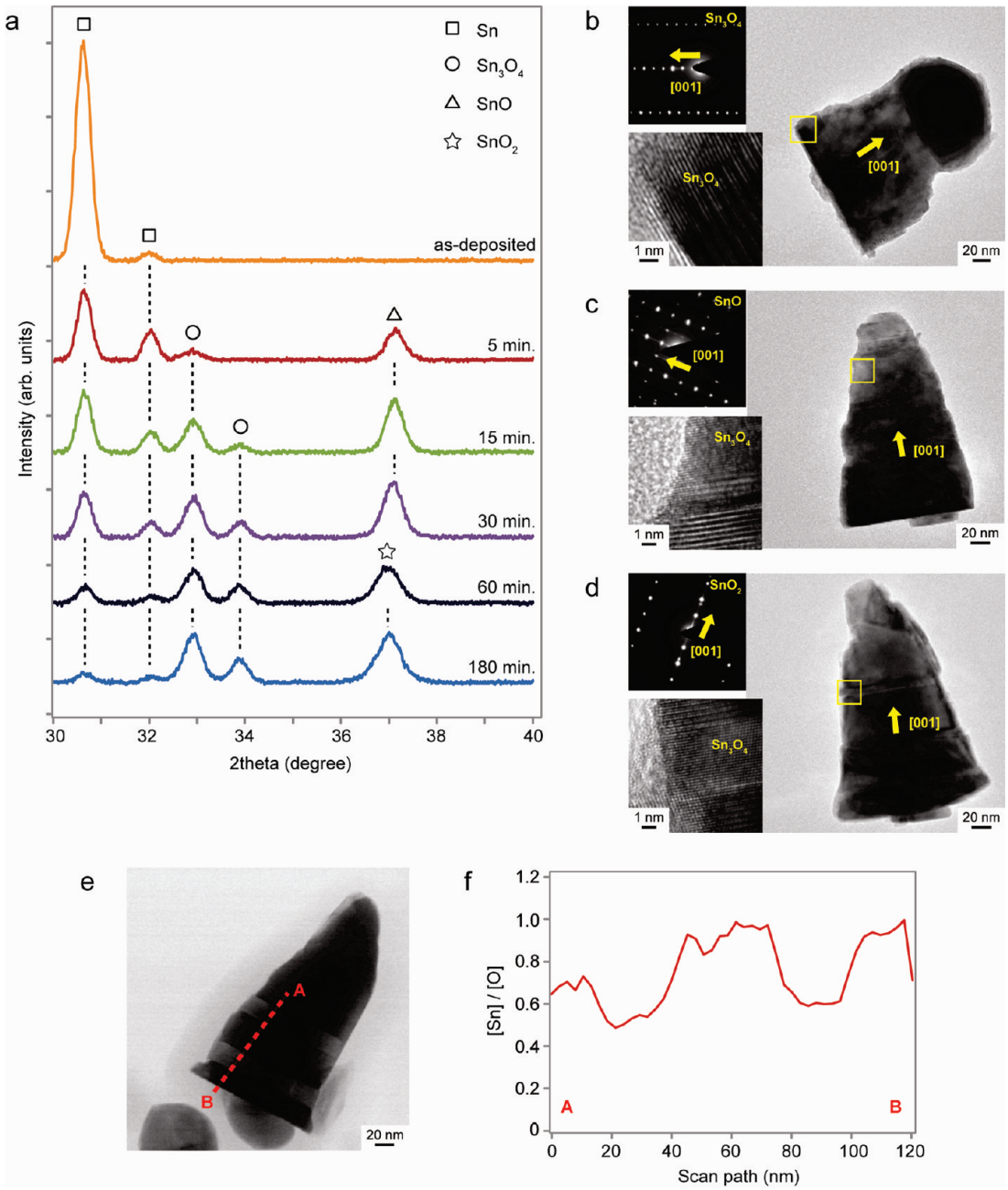

Figure 3. Multiple phases of SnO_x in nanocones. (a) XRD data of SnO_x nanocones grown for different time periods. Sn films were 50 nm thick, and the annealing temperature and oxygen concentration were 300 °C and less than 100 ppm, respectively. (b−d) TEM data of the Sn_3O_4 (b), SnO (c), and SnO_2 (d) nanocones annealed for 15, 180, and 180 min, respectively. The insets are the diffraction patterns and the HRTEM images of the areas indicated by yellow squares. The HRTEM images of c and d show that there are different phases, Sn_3O_4, in the middle of the nanocones. (e) STEM data of the SnO_x nanocone annealed for 180 min. (f) EDS data collected along the red trace from point A to B in panel e.

the annealing temperature and the oxygen concentration results in different nanocone shapes.

The easily fabricated SnO_x nanocones described here show promise for forming an effective anti-reflection layer for photovoltaic devices. The tapering structure of the nanocone leads to a gradual change of refractive index, which is a key factor in enhancing light absorption. In addition, as the absorber layer in solar cells becomes thinner to reduce material costs, this scalable and non-etching technique could be effectively integrated into industrial processes. To demonstrate this, we fabricated SnO_x nanocone arrays on glass and a polycrystalline Si substrate. These SnO_x nanocone arrays were fabricated by annealing a 50 nm thick Sn film at 300 °C for 3 h in the low-oxygen environment and another 3 h in air, sequentially, in order to remove all of the residue of Sn and SnO. On the basis of the XRD data shown in Supporting Information Figure S5, only SnO_2 and Sn_3O_4 remained on the sample. The band gap of SnO_2 is 3.6 eV,[22] thus SnO_2 nanocones are

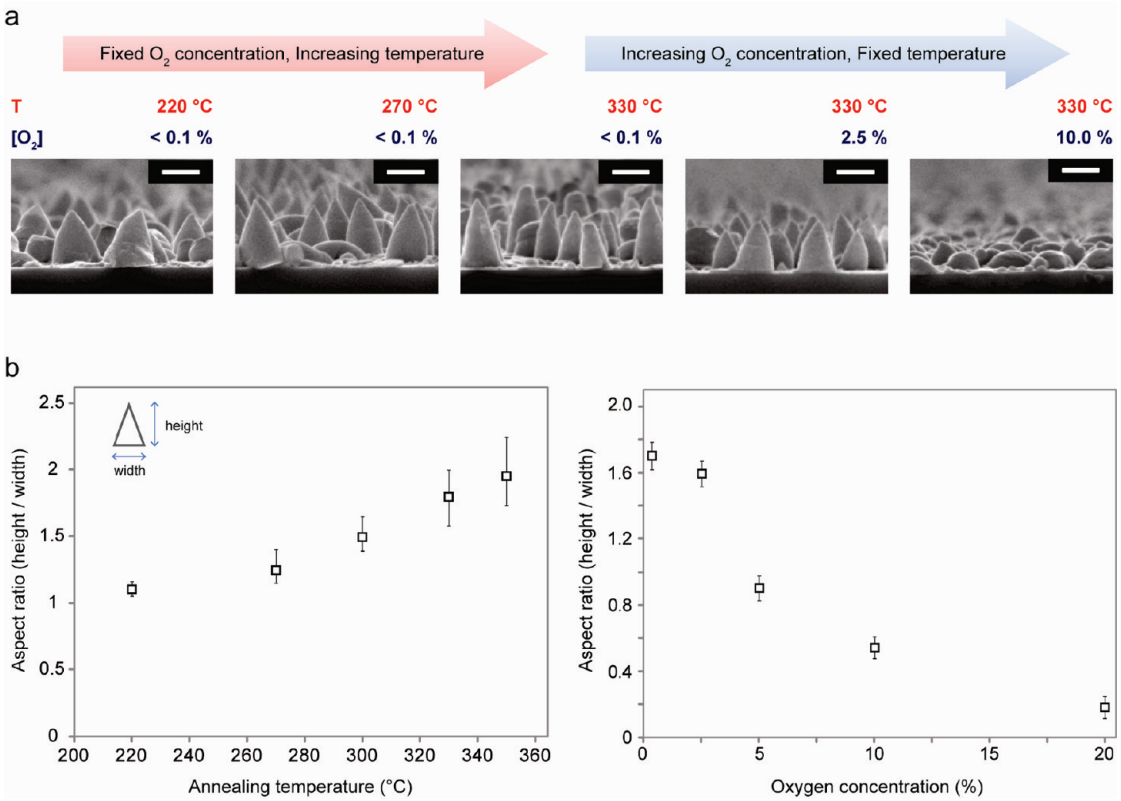

Figure 4. Shape control of SnO_x nanocones. (a) SEM images of SnO_x nanocones grown in environments with different temperatures and oxygen concentrations. All scale bars are 200 nm. (b) Nanocone aspect ratio *versus* annealing temperature and oxygen concentration. Error bars indicate one standard deviation of the aspect ratio measurements of 50 nanocones in each condition.

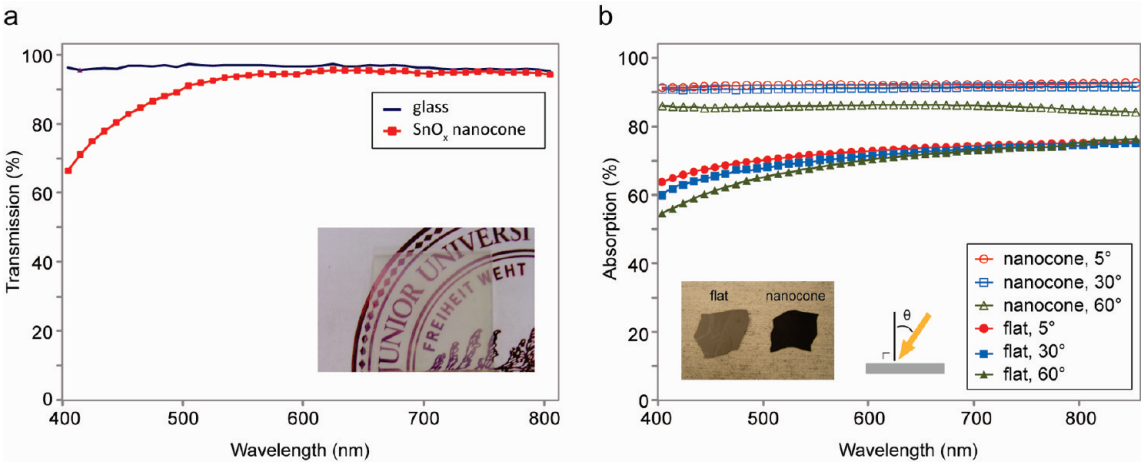

Figure 5. Optical properties of SnO_x nanocone arrays. (a) Transmission measurement data of bare glass and glass with SnO_x nanocones. Inset is the photograph of the glass with SnO_x nanocones formed from a 50 nm thick Sn film. (b) Absorption measurement data of polycrystalline Si substrates with and without SnO_x nanocones. The nanocones were formed from a 50 nm thick Sn film. All of the angle- dependence measurements were conducted by using an integrating sphere.

transparent in the visible range of light (400−850 nm). Even though the band gap of Sn_3O_4 is 2.9 eV,[23] which corresponds to a wavelength of 430 nm, more than 70% of light with that wavelength passed through the glass with nanocones (Figure 5a) because less than half of the surface was covered with SnO_x nanocones (see Supporting Information for details). The light absorption of the polycrystalline Si covered with SnO_x nanocones is increased by over 30% in the 400−850 nm wavelength range compared to the bare substrate (Figure 5b). The angle for the angle-dependence experiment was defined in the inset in Figure 5b. The light absorption of the polycrystalline Si with nanocones tilted to 60° with respect to the incident light is even higher than that of a bare substrate tilted to 5°.

CONCLUSION

We report the growth mechanism of SnO_x nanocones formed through self-catalytic VLS growth at low temperatures. This fabrication method is simple, nondestructive, and scalable over large areas. The anti-reflection properties exhibited by Sn_3O_4/SnO_2 nanocone arrays can be utilized as a low-cost method to increase absorption in photovoltaics. In addition, because the nanocones are transparent and fabricated at low temperatures, they have the potential to be used in the field of nanobiotechnology, especially in the area of neural interfaces.[24,25]

METHODS

Substrate Preparation. All of the substrates on which we deposited Sn were thoroughly cleaned in ultrasonic baths of acetone, methanol, and ethanol for 15 min each before the deposition.

Sn Deposition. An e-beam evaporator was used for Sn deposition. The deposition rates were 5−10 Å/s with a pressure of 10^{-6} Torr.

SnO_x Nanocone Formation at Different Oxygen Partial Pressures. Evaporated Sn films with a thickness of 50 nm on Si substrates were put in a quartz tube and annealed in a furnace. Before annealing, the quartz tube was pumped and purged with a mixture of gas (nitrogen and oxygen) several times. The flow rates of nitrogen and oxygen were controlled by two separate mass flow controllers in order to make low-oxygen environments with 0.1, 2.5, 5, and 10% of oxygen concentrations. The experiments with less than 0.1% of oxygen concentration were conducted in a glovebox. The annealing temperature was between 220 and 450 °C, with a constant ramp rate of 3 °C/s.

Light Absorption Measurement. The light absorption was measured with an integrating sphere (Labsphere). A tungsten lamp coupled to a monochromator was used as a light source, and the sample was mounted at the center of the sphere.

Acknowledgment. This work is based upon work supported as part of the Center on Nanostructuring for Efficient Energy Conversion (CNEEC) at Stanford University, an Energy Frontier Research Center funded by the U.S. Department of Energy, Office of Science, Office of Basic Energy Sciences under Award Number DE-SC0001060. A portion of this work is also supported by the U.S. Department of Energy under the Award Number DE-FG36-08GOI8004. S.J. acknowledges support from the Korea Foundation for Advanced Studies (KFAS) for graduate fellowship. M.T.M. acknowledges support from the National Defense Science and Engineering Graduate Fellowship and the National Science Foundation Graduate Fellowship.

Supporting Information Available: Additional figures and experimental details. This material is available free of charge *via* the Internet at http://pubs.acs.org.

REFERENCES AND NOTES

1. Tsakalakos, L.; Balch, J.; Fronheiser, J.; Korevaar, B. A.; Sulima, O.; Rand, J. Silicon Nanowire Solar Cells. *Appl. Phys. Lett.* **2007**, *91*, 233117/1-3.
2. Kelzenberg, M. D.; Boettcher, S. W.; Petykiewicz, J. A.; Turner-Evans, D. B.; Putnam, M. C.; Warren, E. L.; Spurgeon, J. M.; Briggs, R. M.; Lewis, N. S.; Atwater, H. A. Enhanced Absorption and Carrier Collection in Si Wire Arrays for Photovoltaic Applications. *Nat. Mater.* **2010**, *9*, 239–244.
3. Garnett, E.; Yang, P. Light Trapping in Silicon Nanowire Solar Cells. *Nano Lett.* **2010**, *10*, 1082–1087.
4. Zhu, J.; Yu, Z.; Burkhard, G. F.; Hsu, C.-M.; Connor, S. T.; Xu, Y.; Wang, Q.; McGehee, M.; Fan, S.; Cui, Y. Optical Absorption Enhancement in Amorphous Silicon Nanowire and Nanocone Arrays. *Nano Lett.* **2009**, *9*, 279–282.
5. Zhu, J.; Hsu, C.-M.; Yu, Z.; Fan, S.; Cui, Y. Nanodome Solar Cells with Efficient Light Management and Self-Cleaning. *Nano Lett.* **2010**, *10*, 1979–1984.
6. Xia, F.; Jiang, L. Bio-Inspired, Smart, Multiscale Interfacial Materials. *Adv. Mater.* **2008**, *20*, 2842–2858.
7. Geim, A, K.; Dubonos, S. V.; Grigorieva, I. V.; Novoselov, K. S.; Zhukov, A. A.; Shapoval, S. Y. Microfabricated Adhesive Mimicking Gecko Foot-Hair. *Nat. Mater.* **2003**, *2*, 461–463.
8. Autumn, K.; Sitti, M.; Liang, Y. A.; Peattie, A. M.; Hansen, W. R.; Sponberg, S.; Kenny, T. W.; Fearing, R.; Israelachvili, J. N.; Full, R. J. Evidence for van der Waals Adhesion in Gecko Setae. *Proc. Natl. Acad. Sci. U.S.A.* **2002**, *99*, 12252–12256.
9. Fan, Z.; Razavi, H.; Do, J.; Moriwaki, A.; Ergen, O.; Chueh, Y.; Leu, P. W.; Ho, J. C.; Takahashi, T.; Reichertz, L. A.; *et al.* Three-Dimensional Nanopillar-Array Photovoltaics on Low-Cost and Flexible Substrates. *Nat. Mater.* **2009**, *8*, 648–653.
10. Jeong, S.; Hu, L.; Lee, H. R.; Garnett, E.; Choi, J. W.; Cui, Y. Fast and Scalable Printing of Large Area Monolayer Nanoparticles for Nanotexturing Applications. *Nano Lett.* **2010**, *10*, 2989–2994.
11. Partridge, J. G.; Field, M. R.; Peng, J. L.; Sadek, A. Z.; Kalantar-zadeh, K.; Du Plessis, J.; McCulloch, D. G. Nanostructured SnO_2 Films Prepared from Evaporated Sn and Their Application as Gas Sensors. *Nanotechnology* **2008**, *19*, 125504/1-5.
12. Yin, Y.; Rioux, R. M.; Erdonmez, C. K.; Hughes, S.; Somorjai, G. A.; Alivisatos, A. P. Formation of Hollow Nanocrystals through the Nanoscale Kirkendall Effect. *Science* **2004**, *304*, 711–714.
13. Railsback, J. G.; Johnston-Peck, A. C.; Wang, J.; Tracy, J. B. Size-Dependent Nanoscale Kirkendall Effect During the Oxidation of Nickel Nanoparticles. *ACS Nano* **2010**, *4*, 1913–1920.
14. Fan, H. J.; Scholz, R.; Kolb, F. M.; Zacharias, M.; Gosele, U. Growth Mechanism and Characterization of Zinc Oxide Microcages. *Solid State Commun.* **2004**, *130*, 517–521.
15. Stach, E. A; Pauzauskie, P. J.; Kuykendall, T.; Goldberger, J.; He, R.; Yang, P. Watching GaN Nanowires Grow. *Nano Lett.* **2003**, *3*, 867–869.
16. Morales, A.; Lieber, C. A Laser Ablation Method for the Synthesis of Crystalline Semiconductor Nanowires. *Science* **1998**, *279*, 208–211.
17. Wu, Y.; Yang, P. Direct Observation of Vapor−Liquid−Solid Nanowire Growth. *J. Am. Chem. Soc.* **2001**, *123*, 3165–3166.
18. Choi, W.; Sung, H.; Kim, K.; Cho, J.; Choi, S. Oxidation Process from SnO to SnO_2. *J. Mater. Sci. Lett.* **1997**, *16*, 1551–1554.
19. Fiori, L.; Ricci, E.; Arato, E. Dynamic Surface Tension Measurements on Molten Metal-Oxygen Systems: Model Validation on Molten Tin. *Acta Mater.* **2003**, *51*, 2873–2890.
20. Yuan, Z. F.; Mukai, K.; Takagi, K.; Ohtaka, M.; Huang, W. L.; Liu, Q. S. Surface Tension and Its Temperature Coefficient of Molten Tin Determined with the Sessile Drop Method at Different Oxygen Partial Pressures. *J. Colloid Interface Sci.* **2002**, *254*, 338–345.
21. Saka, H.; Sasaki, K.; Tsukimoto, S.; Arai, S. *In Situ* Observation of Solid−Liquid Interfaces by Transmission Electron Microscopy. *J. Mater. Res.* **2005**, *20*, 1629–1640.
22. Duan, J.; Yang, S.; Liu, H.; Gong, J.; Huang, H.; Zhao, X.; Zhang, R.; Du, Y. Single Crystal SnO_2 Zigzag Nanobelts. *J. Am. Chem. Soc.* **2005**, *127*, 6180–6181.
23. Berengue, O. M.; Simon, R. A.; Chiquito, A. J.; Dalmaschio, C. J.; Leite, E. R.; Guerreiro, H. A.; Guimarães, F. E. G. Semiconducting Sn_3O_4 Nanobelts: Growth and Electronic Structure. *J. Appl. Phys.* **2010**, *107*, 033717/1-4.

24. Fromherz, P. Electrical Interfacing of Nerve Cells and Semiconductor Chips. *Chem. Phys. Chem.* **2002**, *3*, 276–284.
25. Kotov, N. A.; Winter, J. O.; Clements, I. P.; Jan, E.; Timko, B. P.; Campidelli, S.; Pathak, S.; Mazzatenta, A.; Lieber, C. M.; Prato, M.; *et al.* Nanomaterials for Neural Interfaces. *Adv. Mater.* **2009**, *21*, 3970–4004.